Semianalytical Solution for Power-Law Polymer Solution Flow in a Converging Annular Spinneret

Yi-Rui Chen and Liang-Hsun Chen
Dept. of Chemical Engineering, National Taiwan University, Taipei 106, Taiwan

Kuo-Lun Tung
Dept. of Chemical Engineering, National Taiwan University, Taipei 106, Taiwan

R&D Center for Membrane Technology, Chung Yuan Christian University, Chungli 320, Taiwan

Yu-Ling Li
Dept. of Products, Taiwan Textile Research Institute, Tucheng Dist., New Taipei City 243, Taiwan

Yu-Shao Chen and Che-Chia Hu
Dept. of Chemical Engineering, Chung Yuan Christian University, Chungli 320, Taiwan

Ching-Jung Chuang
R&D Center for Membrane Technology, Chung Yuan Christian University, Chungli 320, Taiwan

Dept. of Chemical Engineering, Chung Yuan Christian University, Chungli 320, Taiwan

DOI 10.1002/aic.14875
Published online May 25, 2015 in Wiley Online Library (wileyonlinelibrary.com)

A semianalytical solution for a power-law fluid flowing through a conical annulus was derived to estimate the velocity profile in the axial direction, the shear rate and the elongation rate within a spinneret during the spinning of hollow fiber membranes. The angle coefficient was introduced as a new parameter to account for the effect of radial flow and to modify the governing equation, which initially neglected the effect of radial flow. The results estimated from this semianalytical solution agreed more closely with computational fluid dynamics simulation results than those obtained from the approximate analytical solution in our previous study. By accurately predicting the velocity profile in the axial direction and the shear and elongation rates in a conical annulus, the solution derived in this study is expected to provide a reliable criterion for spinneret design to achieve a specified membrane morphology with a desired performance.
© 2015 American Institute of Chemical Engineers *AIChE J*, 61: 3489–3499, 2015
Keywords: power-law fluid, converging annulus, conical spinneret, hollow fiber membrane, shear rate

Introduction

Membrane separation technologies have become indispensable in chemical industries. Among the various types of membrane modules, hollow fiber membranes are widely used due to their numerous advantages, such as high membrane packing density, high mechanical strength, and back-flushing capabilities. However, the parameters controlling the spinning process of hollow fiber membranes are complicated, and many of these parameters have been investigated to date. In addition to finding the appropriate materials and methods to spin membranes,[1–12] another key issue is the determination of the effect of flow conditions within the spinneret on the membrane morphology and properties.[13–19] Aptel et al.[13] introduced the spinning number, an empirical dimensionless coefficient, to correlate several spinning variables that strongly influence the hydraulic permeability of hollow fiber membranes. Chung et al.[14–19] determined the effects of the shear stress and shear rate within the spinneret on the membrane morphology and properties when spinning hollow fiber membranes using different dope materials. They reported that increasing either the shear rate or the dope extrusion rate enhances the molecular orientation of polymer molecules in dope solutions and leads to higher selectivity but lower permeability. Moreover, Chung et al.[19] also observed a critical shear rate beyond which the membrane performance no longer changed significantly because the molecular orientation induced by the shear rate was offset by the shear-thinning effect of a high-concentration polymer dope. As a result, there exists an optimum shear rate for maximum separation performance, as demonstrated by infrared spectroscopy.[20–22]

In addition to these experimental studies, researchers have also developed analytical models. Fredrickson and Bird[23] derived an analytical solution for a power-law fluid flowing

Additional Supporting Information may be found in the online version of this article.

Correspondence concerning this article should be addressed to K.-L. Tung at kuolun@ntu.edu.tw.

© 2015 American Institute of Chemical Engineers

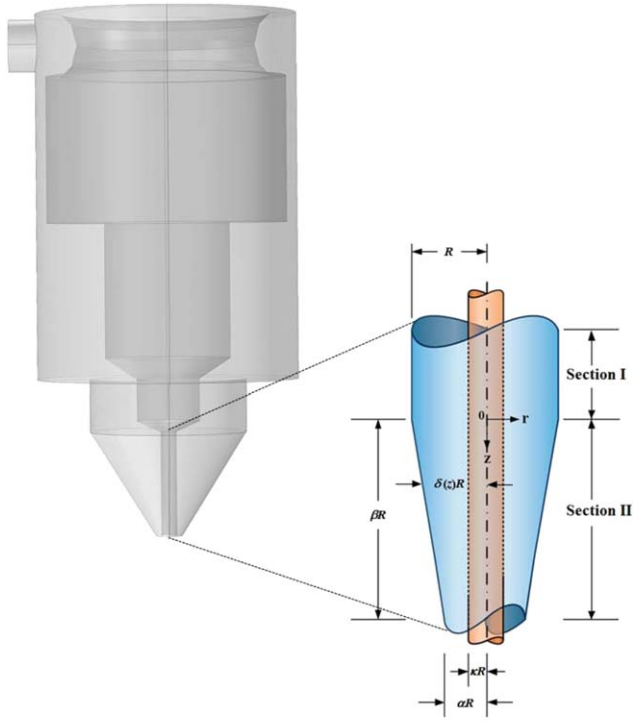

Figure 1. Schematic diagrams of (a) the actual conical annulus spinneret used for the spinning process and (b) the domain of the semianalytical solution derived in this study.

[Color figure can be viewed in the online issue, which is available at wileyonlinelibrary.com.]

through a long cylindrical annulus. Shilton[24] derived flow equations and presented a methodology to establish flow profiles in a spinneret during the spinning of hollow fiber membranes. Wang et al.[25] concluded that the flow angle of the spinneret is another important variable in the spinning processes by showing that hollow fiber membranes spun from a conical spinneret exhibit better separation performance than those spun from a straight one. Widjojo et al.[26] designed several novel spinnerets and applied both Computational fluid dynamics (CFD) methods and experiments to demonstrate that conical spinneret with a flow angle of 60° can reduce flow instability phenomena. Therefore, spinneret designs typically feature a converging cross-section; designs with straight annuli have been found to be inappropriate for predicting general membrane spinning processes. CFD methods can be used to simulate the flow profile in a spinneret during spinning and have been widely applied for designing membrane modules.[27–35] Cao et al.[27] first implemented CFD methods to simulate the flow profiles for a dope solution flowing through spinnerets for three different flow angles. They proposed a hypothetical mechanism in which the elongation rate stretches the polymer chains and enhances chain packing in the outer skin of hollow fiber membranes and the shear rate aligns the polymer chains. Cao et al.[27] concluded that the elongation rate contributes more to the membrane permeability, while the shear rate contributes more to the membrane selectivity. To provide a convenient method for engineers to predict the flow behavior within a spinneret, Tung et al.[33] derived an approximate analytical solution for a power-law fluid flowing through the conical spinneret neglecting the effect of radial flow. Although the results were more accurate than those derived for a straight annulus, neglecting of the effect of radial flow introduced significant error. For a power-law fluid of $n = 1.423$ flowing at a high flow rate in the laminar flow regime in a 60° spinneret, the shear stresses at the outer and inner walls deviated from the CFD simulation results by up to 47% and 21%, respectively.

To the best of our understanding, no efforts have been published on the derivation of analytical solution that accounts for the effect of radial flow in a conical spinneret during spinning processes. By introducing an angle coefficient to account for the effect of radial flow, this study derived a semianalytical solution to accurately estimate the z-velocity profile, elongation rate, and shear rate of power-law fluids flowing through conical spinnerets for different flow angles. These semianalytical results were then compared with CFD simulation results to validate our work.

Theoretical Study

A semianalytical solution and CFD simulation software were utilized to analyze the hydrodynamics of power-law fluids flowing through a conical annulus spinneret as shown in Figure 1. To facilitate the mathematical treatment presented throughout this work, the conical annulus was partitioned into two sections, and several geometrical variables were defined.

Analytical derivation

Geometric Variables. Two dimensionless variables are introduced in an axisymmetric cylindrical coordinate system. The transformation from (r, z) to (ξ, ζ) is as follows

$$\zeta = \frac{z}{R} \text{ and } \xi = \frac{r}{R} \tag{1}$$

The inner radius of the converging annulus is always κR, and the outer radii of the annulus for Section I and the outlet

of Section II are R and αR, respectively. The length of the converging section represented by the multiple radii is βR. The slope ε is defined by two dimensionless variables to describe the converging part of the spinneret. The geometrical variables α, β, and ε are related by

$$\varepsilon = \frac{1-\alpha}{\beta} \tag{2}$$

with the outer radius of Section II assumed to be δR, δ can be expressed as

$$\delta = 1-\varepsilon\zeta \tag{3}$$

Furthermore, δ is a function of ζ, that is, a function of z.

Establishment of the Flow System. The assumptions made in both the theoretical derivation and the simulations are listed as follows: (1) steady state, (2) isothermal, (3) incompressible fluid, (4) laminar flow, (5) power-law fluid, (6) no-slip boundary condition at the walls, (7) two-dimensional (2-D) axisymmetric, and (8) neglecting end-effects.

Derivation of the velocity profile in the axial direction

Section II. The spinneret system is a 2-D axisymmetric annulus where the velocity in the θ-direction is zero. As such, the continuity equation can be simplified as Eq. 4

$$\frac{1}{r}\frac{\partial}{\partial r}(rV_r)+\frac{\partial V_z}{\partial z}=0 \tag{4}$$

For the momentum balance, the equation of motion presented in Eq. 5 is employed

$$\frac{\partial}{\partial t}(\rho v)+\nabla\cdot(\rho vv)=-\nabla P-(\nabla\cdot\tau)+\rho g \tag{5}$$

Assuming a negligible gravity effect, the polymer liquid in the spinneret system flows so slowly that the inertia terms in the equation of motion can be neglected; the equation of motion can be simplified as Eq. 6

$$0=-\nabla P-(\nabla\cdot\tau) \tag{6}$$

The governing equation of Eq. 6 in the z-direction is shown in Eq. 7

$$0=-\frac{\partial P}{\partial z}-\left[\frac{1}{r}\frac{\partial}{\partial r}(r\tau_{rz})+\frac{\partial}{\partial z}(\tau_{zz})\right] \tag{7}$$

The generalized power-law model is applied for the polymer solutions, and the deformation relationships required to solve Eq. 7 are as follows

$$\tau_{rz}=-m\left[2\left(\frac{\partial V_r}{\partial r}\right)^2+\left(\frac{\partial V_z}{\partial r}+\frac{\partial V_r}{\partial z}\right)^2+2\left(\frac{V_r}{r}\right)^2+2\left(\frac{\partial V_z}{\partial z}\right)^2\right]^{\frac{n-1}{2}}\left(\frac{\partial V_z}{\partial r}+\frac{\partial V_r}{\partial z}\right) \text{ and} \tag{8}$$

$$\tau_{zz}=-m\left[2\left(\frac{\partial V_r}{\partial r}\right)^2+\left(\frac{\partial V_z}{\partial r}+\frac{\partial V_r}{\partial z}\right)^2+2\left(\frac{V_r}{r}\right)^2+2\left(\frac{\partial V_z}{\partial z}\right)^2\right]^{\frac{n-1}{2}}\left(2\frac{\partial V_z}{\partial z}\right) \tag{9}$$

However, because both V_z and V_r are nonzero, the nonlinear partial differential equations cannot be solved, even when utilizing the continuity equation. V_r is "temporarily assumed" to be zero, and $\frac{\partial V_z}{\partial z}$ is neglected according to the continuity equation. As a result, Eqs. 7 and 8 can be simplified as

$$\frac{\partial}{\partial r}(r\tau_{rz})=r\left(-\frac{dP}{dz}\right) \text{ and} \tag{10}$$

$$\tau_{rz}=-m\left|\frac{dV_z}{dr}\right|^{n-1}\left(\frac{dV_z}{dr}\right), \text{ respectively} \tag{11}$$

The deviations from this assumption are corrected in later sections.

The variable λR is introduced to designate the position of maximum z-velocity; it is an underdetermined constant in Section I and varies with ζ in Section II. By integrating Eq. 10 with the condition shown in Eq. 12

$$r=\lambda R,\quad \frac{dV_z}{dr}=0, \tag{12}$$

we obtain Eq. 13 as

$$\tau_{rz}=\frac{1}{2}\left(-\frac{dP}{dz}\right)\left(r-\frac{(\lambda R)^2}{r}\right) \tag{13}$$

The ratio of the shear stress (τ_{rz}) obtained from the CFD analytical solution (with the effect of radial flow) to that from the approximate analytical analysis (without the effect of radial flow) was observed to be approximately constant at the inner and outer walls for spinnerets for various flow angles. As a result, the angle coefficient ϕ shown in Eq. 14 is introduced to include the effect of the radial flow on shear stress as

$$\phi=A\psi+B \tag{14}$$

This correcting shear stress ratio is used to modify the governing equation expressed in Eq. 13. The parameter ψ is a new dimensionless variable defined in Eq. 15 to eliminate the radial dimension of the inner tube of the annulus as

$$\psi=\frac{\xi-\kappa}{\delta_{(\zeta)}-\kappa} \tag{15}$$

Relative to the straight annulus, the parameter B includes the effect of the radial flow on the shear stress ratio at the inner wall, and the parameter A includes the effect of the radial flow on the shear stress ratio linearly from the inner wall to the outer wall. For a straight annulus, the angle coefficient can be reduced to unity. To facilitate the following calculation, Eq. 13 is multiplied by the angle coefficient to the power of n as shown in Eq. 16

$$\tau_{rz}=\frac{1}{2}\left(-\frac{dP}{dz}\right)(\boldsymbol{A\psi}+\boldsymbol{B})^n\left(r-\frac{(\lambda R)^2}{r}\right) \tag{16}$$

The system depends on six variables: the volumetric flow rate, the geometrical variables of the spinneret (κ, ξ, ζ, and ε) and the power law n-index. In the tube flow system, the volumetric flow rate is inherent in $(-dP/dz)$ and m and is not dependent on the angle coefficient. Therefore, it is reasonable to hypothesize that ε and n are included in values A and B. Subsequently, A and B are determined through regression analysis as Eqs. 17 and 18; the results of computations used for the regression are listed in Supporting Information 1 in a separate file

$$A=-3.286\varepsilon^{2.317}n^{-0.293} \text{ and} \tag{17}$$

$$B=2.898\varepsilon^{2.979}n^{-0.381}+1 \tag{18}$$

By substituting Eq. 11 into Eq. 16, the z-velocity profile across the spinneret is solved with the boundary conditions $V_z=0$ at both $r=\kappa R$ and $r=R$, which leads to

$$V_{z,II}=R\left[\frac{R}{2m}\left(-\frac{dP}{dz}\right)\right]^s\int_\kappa^\xi(\boldsymbol{A\psi}+\boldsymbol{B})\left(\frac{\lambda^2}{\xi}-\xi\right)^s d\xi \tag{19a}$$
for $\kappa\le\xi\le\lambda$ and

$$V_{z,II}=R\left[\frac{R}{2m}\left(-\frac{dP}{dz}\right)\right]^s\int_\xi^{\delta_{(\zeta)}}(\boldsymbol{A\psi}+\boldsymbol{B})\left(\xi-\frac{\lambda^2}{\xi}\right)^s d\xi \tag{19b}$$
for $\lambda\le\xi\le\delta_{(\zeta)}$

where $s=1/n$. By equating Eq. 19a with Eq. 19b, the parameter λ is numerically solved as

$$\int_\kappa^\lambda(\boldsymbol{A\psi}+\boldsymbol{B})\left(\frac{\lambda^2}{\xi}-\xi\right)^s d\xi=\int_\lambda^{\delta_{(\zeta)}}(\boldsymbol{A\psi}+\boldsymbol{B})\left(\xi-\frac{\lambda^2}{\xi}\right)^s d\xi \tag{20}$$

The volumetric flow rate is calculated by integrating the z-velocity profile across the annulus as Eq. 21

$$\begin{aligned}Q_{II}&=2\pi\int_{\kappa R}^{\delta R}V_z r dr=2\pi\int_{\kappa R}^{\lambda R}V_z r dr+2\pi\int_{\lambda R}^{\delta R}V_z r dr\\&=\pi R^3\left[\frac{R}{2m}\left(-\frac{dP}{dz}\right)\right]^s\int_\kappa^\delta(\boldsymbol{A\psi}+\boldsymbol{B})\left|\lambda^2-\xi^2\right|^{s+1}\xi^{-s}d\xi\end{aligned} \tag{21}$$

Rearranging Eq. 21 can obtain another expression of volumetric flow rate vs. applying pressure as

$$\left[\frac{R}{2m}\left(-\frac{dP}{dz}\right)\right]^s=\frac{Q_{II}}{\pi R^3}\frac{1}{\int_\kappa^\delta(\boldsymbol{A\psi}+\boldsymbol{B})|\lambda^2-\xi^2|^{s+1}\xi^{-s}d\xi} \tag{22}$$

Given all the systematic variables, the result of Eq. 22 is substituted into Eqs. 19a and 19b to solve the z-velocity profile.

Section I. Section I is the special case of Section II when δ is given the value of unity and the z-velocity in Section I is expressed as follows

$$V_{z,I}=R\left[\frac{R}{2m}\left(-\frac{dP}{dz}\right)\right]^s\int_\kappa^\xi\left(\frac{\lambda^2}{\xi}-\xi\right)^s d\xi,\ \kappa\le\xi\le\lambda \text{ and} \tag{23a}$$

$$V_{z,I}=R\left[\frac{R}{2m}\left(-\frac{dP}{dz}\right)\right]^s\int_\xi^1\left(\xi-\frac{\lambda^2}{\xi}\right)^s d\xi,\ \lambda\le\xi\le\delta_{(\zeta)} \tag{23b}$$

The variable λ in Section I is numerically solved as

$$\int_\kappa^\lambda\left(\frac{\lambda^2}{\xi}-\xi\right)^s d\xi=\int_\lambda^1\left(\xi-\frac{\lambda^2}{\xi}\right)^s d\xi \tag{24}$$

The volumetric flow rate in Section I is expressed as

$$\begin{aligned}Q_I&=2\pi\int_{\kappa R}^{\delta R}V_z r dr=2\pi\int_{\kappa R}^{\lambda R}V_z r dr+2\pi\int_{\lambda R}^{R}V_z r dr\\&=\pi R^3\left[\frac{R}{2m}\left(\frac{dP}{dz}\right)\right]^s\int_\kappa^1|\lambda^2-\zeta^2|^{s+1}\zeta^{-s}d\zeta\end{aligned} \tag{25}$$

Details of the derivation of Eq. 25 are supplied in Supporting Information 2 in a separated file.

Derivation of the shear rates

Shear rate is defined as the derivative of axial z-velocity with respect to r

$$\text{Shear rate}=\frac{\partial V_z}{\partial r} \tag{26}$$

Section II. Differentiating V_z in Eqs. 19a and 19b with respect to r gives

$$\begin{aligned}\left|\frac{dV_z}{dr}\right|&=\left[\frac{R}{2m}\left(-\frac{dP}{dz}\right)\right]^s(\boldsymbol{A\psi}+\boldsymbol{B})\left(\xi-\frac{\lambda^2}{\xi}\right)^s\\&=\frac{Q}{\pi R^3}\frac{(\boldsymbol{A\psi}+\boldsymbol{B})\left(\xi-\frac{\lambda^2}{\xi}\right)^s}{\int_\kappa^\delta(\boldsymbol{A\psi}+\boldsymbol{B})|\lambda^2-\xi^2|^{s+1}\xi^{-s}d\xi}\end{aligned}\quad \text{for } \kappa\le\xi\le\lambda \text{ and} \tag{27a}$$

$$\begin{aligned}\left|\frac{dV_z}{dr}\right|&=\left[\frac{R}{2m}\left(-\frac{dP}{dz}\right)\right]^s(\boldsymbol{A\psi}+\boldsymbol{B})\left(\xi-\frac{\lambda^2}{\xi}\right)^s\\&=\frac{Q}{\pi R^3}\frac{(\boldsymbol{A\psi}+\boldsymbol{B})\times\left(\xi-\frac{\lambda^2}{\xi}\right)^s}{\int_\kappa^\delta(\mathrm{A\psi}+\mathrm{B})|\lambda^2-\xi^2|^{s+1}\xi^{-s}d\xi}\end{aligned}\quad \text{for } \lambda\le\xi\le\delta_{(\zeta)} \tag{27b}$$

The local shear rates at the inner and outer walls in Section II are thus

$$\begin{aligned}\left|\frac{dV_z}{dr}\right|_{r=\kappa R}&=\left[\frac{R}{2m}\left(-\frac{dP}{dz}\right)\right]^s(\boldsymbol{A\psi}+\boldsymbol{B})\left(\kappa-\frac{\lambda^2}{\kappa}\right)^s\\&=\frac{Q}{\pi R^3}\frac{(\boldsymbol{A\psi}+\boldsymbol{B})\left(\kappa-\frac{\lambda^2}{\kappa}\right)^s}{\int_\kappa^\delta(\boldsymbol{A\psi}+\boldsymbol{B})|\lambda^2-\xi^2|^{s+1}\xi^{-s}d\xi}\end{aligned}\quad \text{for } \kappa\le\xi\le\lambda \text{ and} \tag{28a}$$

$$\begin{aligned}\left|\frac{dV_z}{dr}\right|_{r=\delta_{(\zeta)}R}&=\left[\frac{R}{2m}\left(-\frac{dP}{dz}\right)\right]^s(\boldsymbol{A\psi}+\boldsymbol{B})\left(\delta-\frac{\lambda^2}{\delta}\right)^s\\&=\frac{Q}{\pi R^3}\frac{(\boldsymbol{A\psi}+\boldsymbol{B})\times\left(\delta-\frac{\lambda^2}{\delta}\right)^s}{\int_\kappa^\delta(\boldsymbol{A\psi}+\boldsymbol{B})|\lambda^2-\xi^2|^{s+1}\xi^{-s}d\xi}\end{aligned}\quad \text{for } \lambda\le\xi\le\delta_{(\zeta)} \tag{28b}$$

Section I. Section I is the special case of section II when δ is given the value of unity and the shear rate is expressed as follows

$$\begin{aligned}\left|\frac{dV_z}{dr}\right|&=\left[\frac{R}{2m}\left(-\frac{dP}{dz}\right)\right]^s\left(\xi-\frac{\lambda^2}{\xi}\right)^s\\&=\frac{Q}{\pi R^3}\frac{\left(\xi-\frac{\lambda^2}{\xi}\right)^s}{\int_\kappa^1|\lambda^2-\xi^2|^{s+1}\xi^{-s}d\xi}\end{aligned}\quad \text{for } \kappa\le\xi\le\lambda \text{ and} \tag{29a}$$

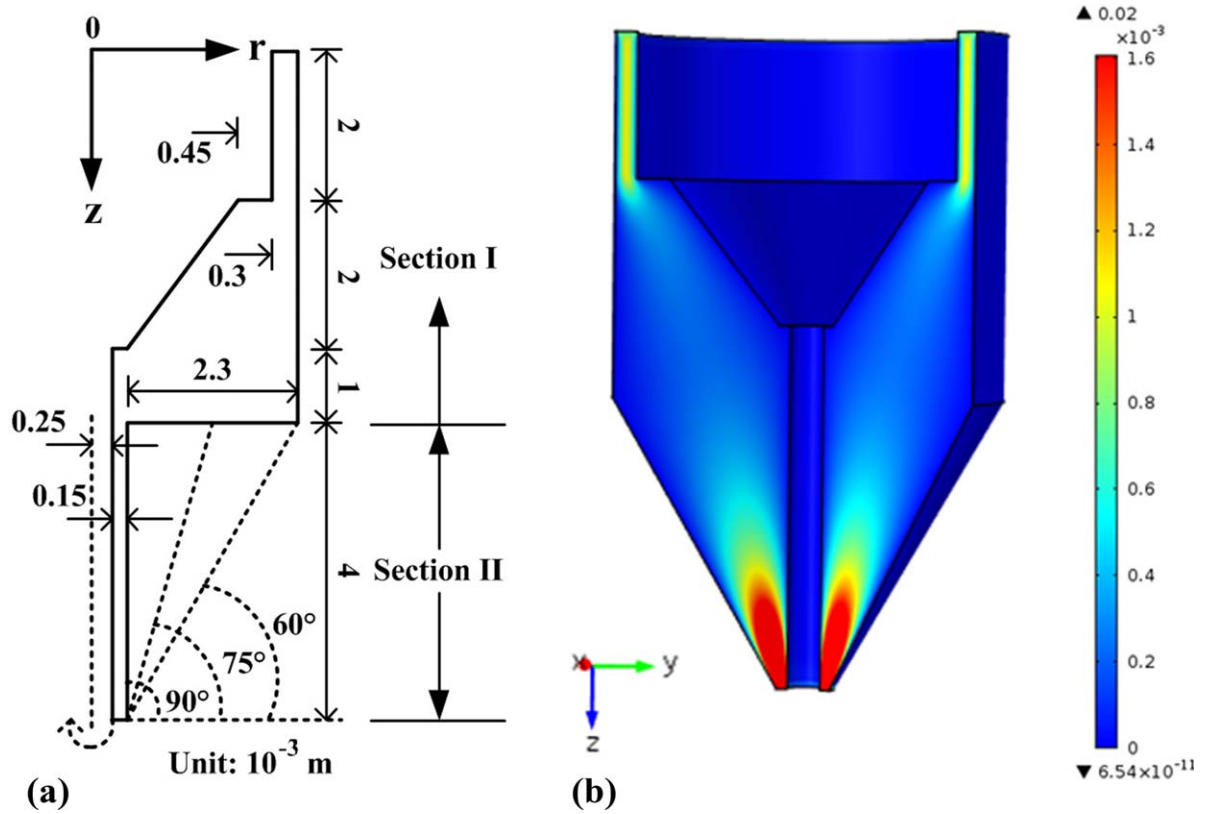

Figure 2. Schematic diagram of the conical annulus spinneret: (a) three real 2-D simulation systems and (b) real three-dimensional simulation system of a 60° spinneret.

[Color figure can be viewed in the online issue, which is available at wileyonlinelibrary.com.]

$$\left|\frac{dV_z}{dr}\right| = \left[\frac{R}{2m}\left(-\frac{dP}{dz}\right)\right]^s \left(\xi - \frac{\lambda^2}{\xi}\right)^s = \frac{Q}{\pi R^3}\frac{\left(\xi - \frac{\lambda^2}{\xi}\right)^s}{\int_\kappa^1 |\lambda^2 - \xi^2|^{s+1}\xi^{-s}d\xi} \quad \text{for } \lambda \le \xi \le \delta_{(\zeta)} \quad (29b)$$

The local shear rates at the inner and outer walls in Section I are thus

$$\left|\frac{dV_z}{dr}\right|_{r=\kappa R} = \left[\frac{R}{2m}\left(-\frac{dP}{dz}\right)\right]^s \left(\kappa - \frac{\lambda^2}{\kappa}\right)^s = \frac{Q}{\pi R^3}\frac{\left(\kappa - \frac{\lambda^2}{\kappa}\right)^s}{\int_\kappa^1 |\lambda^2 - \xi^2|^{s+1}\xi^{-s}d\xi} \quad \text{for } \kappa \le \xi \le \lambda \text{ and} \quad (30a)$$

$$\left|\frac{dV_z}{dr}\right|_{r=R} = \left[\frac{R}{2m}\left(-\frac{dP}{dz}\right)\right]^s (1-\lambda^2)^s = \frac{Q}{\pi R^3}\frac{(1-\lambda^2)^s}{\int_\kappa^1 |\lambda^2 - \xi^2|^{s+1}\xi^{-s}d\xi} \quad \text{for } \lambda \le \xi \le \delta_{(\zeta)} \quad (30b)$$

Given all the systematic variables (r, z, n, Q, R, αR, βR, and κR), the equations above are used to calculate the shear rate distribution in the converging part of a spinneret. First, the variable λ is determined according to Eq. 20. Second, the overall z-velocity profile is obtained from both Eqs. 19a and 19b. Finally, the shear rates at the inner and outer walls are calculated from Eqs. 28a and 28b, respectively. Details of MATLAB program modeling calculation are given as a Supporting Information 3 in a separated file.

Calculation of the Elongation Rate. The z-velocity profile varies with converging cross-section of Section II. Elongation rate is defined as the derivative of axial z-velocity with respect to z

$$\text{Elongation rate} = \frac{\partial V_z}{\partial z} \quad (31)$$

Axial velocities V_z in Eqs. 19a and 19b are differentiated with respect to z for the elongation rate distribution in Section II; however, it is an arduous task since $(-dP/dz)$ and λ in Eqs. 19a and 19b are also the function of z. As a result, this study applies the definition of differentiation in Eq. 32 to simplify the convoluted equations, dividing the control volumes infinitesimally to calculate the elongation rate using

Table 1. Dimensions of a Spinneret with a Converging Cross-Section

Variables	Values (mm)
R (60°)	2.70
R (75°)	1.47
R (90°)	0.40
αR	0.40
βR	4.00
κR	0.25

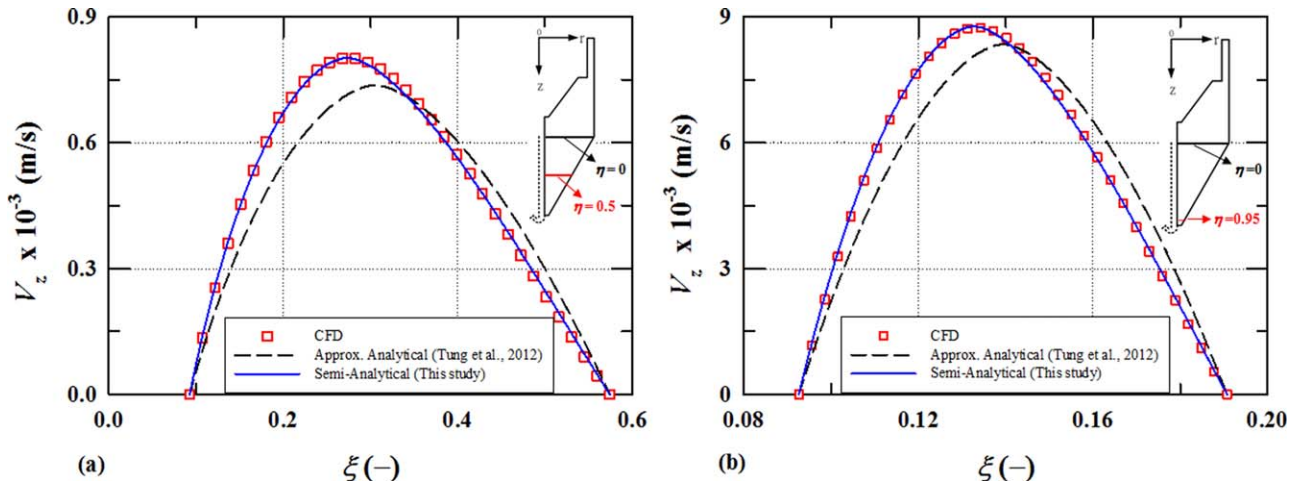

Figure 3. Comparison between the analytical solutions and CFD simulations for the *z*-velocity profile in a conical spinneret with a flow angle of 60° at the axial position where (a) $\eta = 0.5$ and (b) $\eta = 0.95$ ($n = 1.423$, $Q = 0.2$ mL/min).

[Color figure can be viewed in the online issue, which is available at wileyonlinelibrary.com.]

$$\frac{dV_z}{dz} = \lim_{z_1 \to z_2} \frac{V_{z1} - V_{z2}}{z_1 - z_2} \tag{32}$$

Both shear rate and elongation rate distributions calculated here are further compared with CFD simulation results in the following sections. The results are crucial for both quantitative and qualitative analyses during hollow fiber membrane spinning processes.

Flow system and numerical calculation

To validate the semianalytical solution, the commercial CFD software package (ANSYS Fluent®) was used to calculate the velocity profile, elongation rate and shear rate for the power-law fluids in a spinneret during spinning processes. The flow field in the spinneret is considered ideally axisymmetric and reasonably simplified into 2-D planar form to create meshes of high quality using GAMBIT.

The essential details of CFD simulation including general conservation equations, boundary conditions, physical properties of the dope solution, and the iterations are described in our previous work.[33] The steps for CFD simulation are listed as follows. First, general conservation equations in Eq. 4 and Eq. 6 are discretized into algebraic equations. Second, the boundary conditions are defined: (1) inlet velocity: $V_z = V_z$ and $V_r = 0$, (2) outlet pressure: 101,325 Pa, (3) spinneret walls: $V_z = V_r = 0$. Third, physical properties of dope solution are input: (1) dope solution with a density of 1,186.5 kg/m^3 contains 37% polyethersulfone (PES) with a molecular weight of 15,000 in N-methyl-2-pyrrolidone, (2) incompressible fluid with a volumetric flow rate of 0.2 mL/min, (3) ambient temperature, (4) gravitational acceleration of 9.8 m/s^2 acts along the *z*-axis, (5) relationship between shear stress and shear rate of dope solution can be described by a simple power-law expression in Eq. 33

$$\tau = 129.66\ \dot{\gamma}^{1.423} \tag{33}$$

Finally, the sum of the normalized residuals for all variables converges to less than 1×10^{-4} within 5,000 iterations.

Results and Discussion

The semianalytical results for spinnerets at different flow angles are compared with the CFD simulation results and the approximate analytical results derived by Tung et al.[33] The performance of a hollow fiber predicted by the derived semianalytical solution has also been compared with the experimental data reported by Cao et al.[27] to validate the theoretical work derived in this study. The spinneret models are illustrated in Figure 2, and the dimensions of the spinnerets are listed in Table 1.

Axial velocity profiles within the converging section

Figure 3 compares the analytical solutions and CFD simulations for the *z*-velocity profile in a real conical spinneret at a

Table 2. Wall Shear Rate in a Conical Spinneret for Flow Angles of 60°: (a) Inner Wall and (b) Outer Wall ($n = 1.423$, $Q = 0.2$ mL/min)

η	CFD	Approx. Analytical[33]	|Error%|[33]	Semianalytical (This Study)	|Error%| (This Study)
(a) Inner Wall					
0.00	0.77	0.60	22.01	0.80	3.38
0.10	0.98	0.77	21.94	1.02	3.57
0.20	1.29	1.01	21.85	1.34	3.81
0.30	1.74	1.36	21.89	1.81	3.85
0.40	2.45	1.92	21.90	2.55	3.98
0.50	3.65	2.85	21.86	3.80	4.13
0.60	5.85	4.58	21.74	6.11	4.37
0.70	10.47	8.21	21.54	10.96	4.67
0.80	22.33	17.60	21.17	23.47	5.09
0.90	66.76	53.04	20.56	70.50	5.60
0.95	150.17	120.14	20.00	159.24	6.04
0.98	282.10	234.74	16.79	310.25	9.98
1.00	476.72	420.68	11.76	554.81	16.38
(b) Outer Wall					
0.00	−0.09	−0.27	213.45	−0.21	136.80
0.10	−0.24	−0.36	49.65	−0.27	12.96
0.20	−0.34	−0.50	46.21	−0.38	10.83
0.30	−0.48	−0.70	47.07	−0.53	10.41
0.40	−0.71	−1.04	47.32	−0.78	10.45
0.50	−1.11	−1.63	47.34	−1.22	10.17
0.60	−1.89	−2.79	47.36	−2.07	9.70
0.70	−3.63	−5.35	47.18	−3.96	9.07
0.80	−8.45	−12.42	46.96	−9.14	8.23
0.90	−28.11	−41.21	46.57	−30.07	6.97
0.95	−67.44	−99.03	46.84	−71.82	6.49
0.98	−140.25	−201.47	43.66	−145.48	3.73
1.00	−329.10	−372.21	13.10	−267.83	18.62

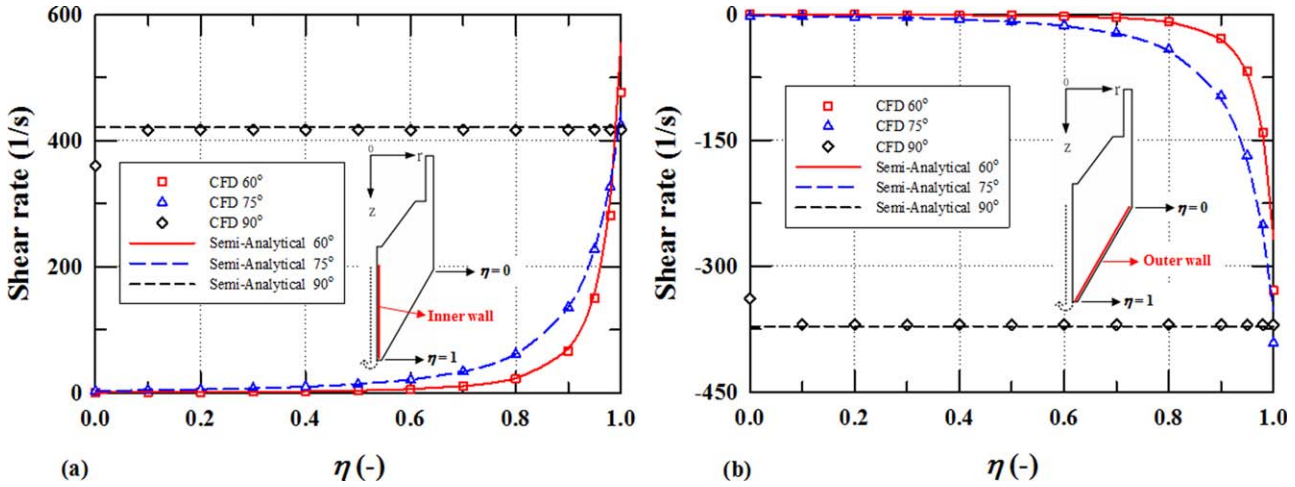

Figure 4. Effect of various flow angles on the shear rate distribution in a conical spinneret: (a) inner wall and (b) outer wall ($n = 1.423$, $Q = 0.2$ mL/min).

[Color figure can be viewed in the online issue, which is available at wileyonlinelibrary.com.]

flow angle of 60°. Because the annulus spinneret is not a single vertical cylinder, the z-velocity profile is not a symmetric parabola. Instead, the maximum z-velocity occurs close to the inner wall due to the smaller frictional area in which the fluid flow is less retarded. As the fluid passes through the conical spinneret, the flow rate increases and the z-velocity profile in the flow direction changes due to the decreasing cross-sectional area. These phenomena are more significant when there is a stronger converging effect in the spinneret.

The z-velocity profiles within Section II derived from Eqs. 19a and 19b agree well with the CFD simulation results, indicating that the modified z-velocity profiles feature accurate positions of the maximum z-velocity and accurate maximum values. According to Eq. 4, which relates V_r and V_z, the accurate z-velocity values confirm the accuracy of the r-velocity values. This indicates that the angle coefficient introduced in this study effectively accounts for the effect of radial flow.

Effect of various flow angles

In this study, the semianalytical results for three angles (i.e., 90°, 75°, and 60°) were considered to find the optimal angle design for spinnerets. The physical properties of the dope solution along the z-direction are discussed in this section. Because the values of R vary with the spinneret angle, a dimensionless variable η is defined in Eq. 34 to eliminate the angle effect and unify the basis of comparison for Section II as

$$\eta = \frac{z}{\beta R} \tag{34}$$

Discussion of the Shear Rate. The increasing shear rate aligns the irregular polymer chains in the flow direction and packs them more densely, enhancing the membrane selectivity. However, excessively high shear rates damage the hollow fiber membranes. Therefore, it is necessary to determine the relationship between the shear rate and the systematic variables.

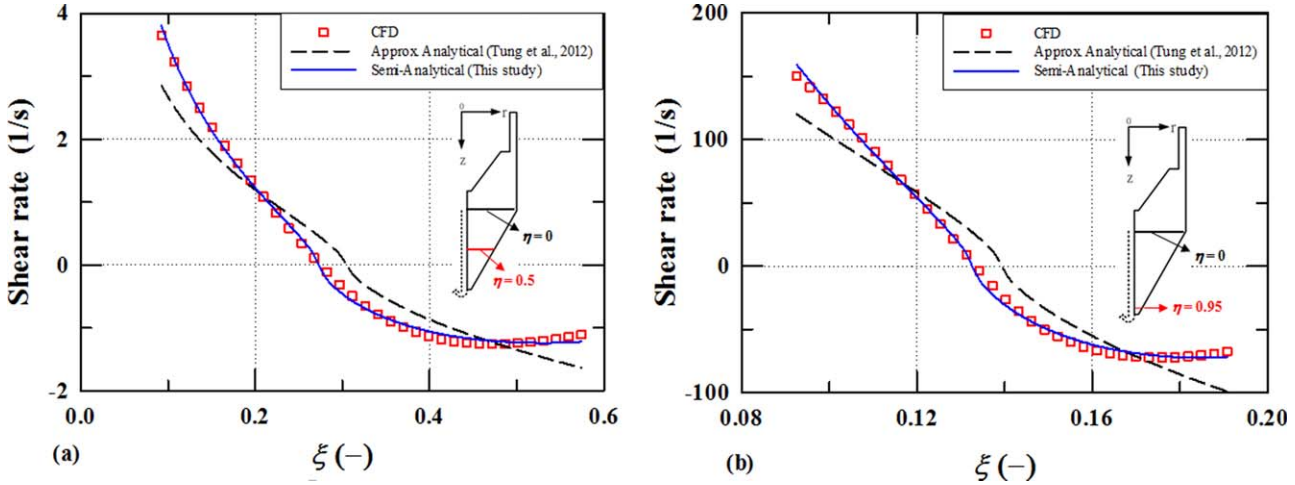

Figure 5. Comparison between the analytical solutions and CFD simulations for the shear rate distribution in a conical spinneret with a flow angle of 60° at the axial position where (a) $\eta = 0.5$ and (b) $\eta = 0.95$ ($n = 1.423$, $Q = 0.2$ mL/min).

[Color figure can be viewed in the online issue, which is available at wileyonlinelibrary.com.]

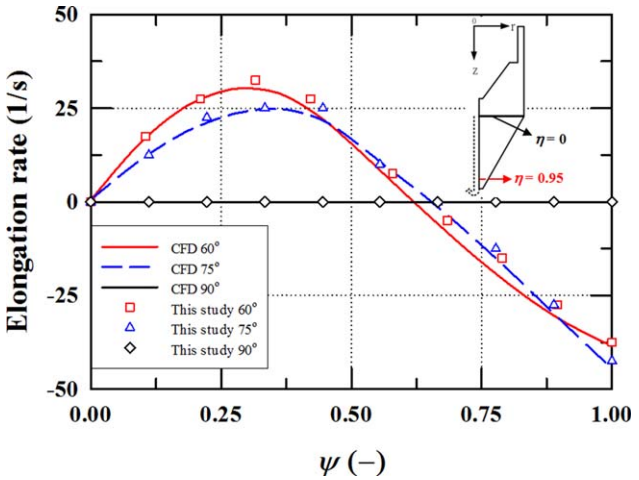

Figure 6. Effect of various flow angles on the elongation rate at the exit of a conical spinneret where $\eta = 0.95$ ($n = 1.423$, $Q = 0.2$ mL/min).

[Color figure can be viewed in the online issue, which is available at wileyonlinelibrary.com.]

Table 2 shows the analytical and CFD results along the z-axis at the inner and outer walls of a conical spinneret. The semianalytical results for the shear rate obtained in this study agree more closely with the CFD simulated results than the model that neglects the effect of radial flow.[33] From the results shown in Table 2, the average deviations of shear stresses derived from the approximate analytical solution reached 47% and 21% at the outer and inner walls, respectively, while the wall shear stresses derived in this study deviated from the CFD simulation results by approximately 10%. The significant discrepancy at the entrance ($\eta = 0$) is due to a sudden converging effect not considered in the analytical solution. The deviation at the spinneret outlet ($\eta = 1$) is primarily due to the discontinuous interface between the liquid and the gas in the CFD simulation.

Figure 4 illustrates the shear rate distributions along the z-axis at the inner and outer walls of the spinnerets for different flow angles. The shear rates at the inner and outer walls decrease as the flow angle decreases because the cross-section at the entrance of Section II is larger for spinnerets with smaller flow angles, as shown in Figure 2. This smaller cross-section induces a greater shear rate at the entrance of the converging section. As a result, the flow angle of the spinneret affects the flow pattern and the rheological properties of the polymer solutions inside the spinneret.

Figure 5 illustrates the shear rate profiles across two cross-sections of the spinneret. The horizontal axis represents dimensionless length, and the vertical axis represents the shear rate. The results in this study are in better agreement with the CFD results than the results of the model that neglects the effect of radial flow.[33] This finding confirms that the highest magnitude of shear rates occur at the inner and outer walls of the spinneret.

Discussion of the Elongation Rate. The elongation rate is an important factor in a spinneret system because an increase in the elongation rate can prevent polymer chains from coiling.

Figure 6 shows the effect of flow angles on the elongation rate at the outlet of the converging section. For fluid passing through a 90° straight annulus, the elongation rate vanishes because the z-velocity profile does not vary along the flow direction. When the fluid passes through a converging annulus, the decreasing area increases the flow rate and induces a z-velocity change in the z-direction. Additionally, a smaller flow angle influences the elongation rate more strongly because the converging effect becomes more pronounced. Although the elongation rate increases and the shear rate decreases as the converging effect becomes more prominent, membranes with excellent separation performances can still be designed if the optimum balance between the elongation rate and shear rate is found.

Effect of various flow rates

Discussion of the Shear Rate at the Inner and Outer Walls. According to the semianalytical shear rate solutions shown in Eqs. 27a and 27b, the shear rate is proportional to the flow rate under the laminar flow conditions. To eliminate the effect of the flow rate, we take the ratio of the shear rate to the flow rate. Figure 7 shows that the ratio profiles along the z-direction at the inner and outer walls remain identical to the flow rate as it varies. Given the shear rate profile for a given

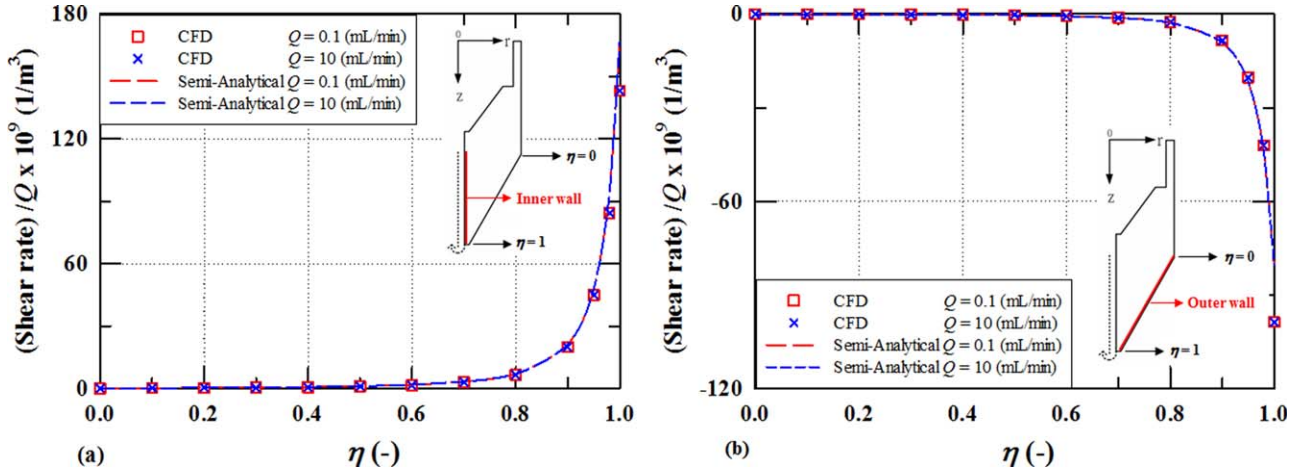

Figure 7. Effect of various dope fluid flow rates on the shear rate distribution in a conical spinneret: (a) inner wall and (b) outer wall (60°, $n = 1.423$).

[Color figure can be viewed in the online issue, which is available at wileyonlinelibrary.com.]

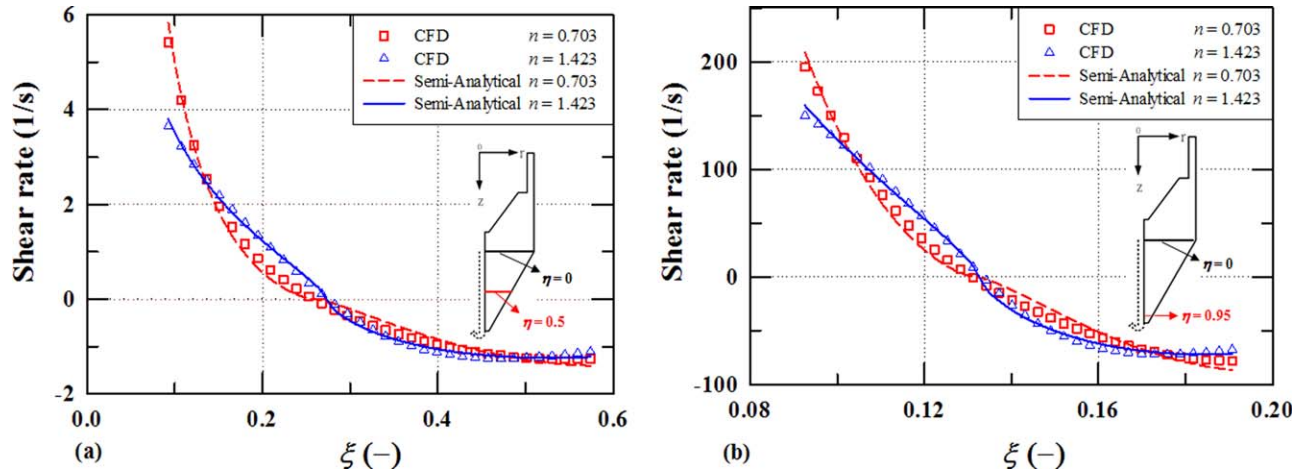

Figure 8. Shear rate distribution for various n values in a conical spinneret with a flow angle of 60° at the axial position where (a) $\eta = 0.5$ and (b) $\eta = 0.95$ ($n = 1.423$, $Q = 0.2$ mL/min).

[Color figure can be viewed in the online issue, which is available at wileyonlinelibrary.com.]

flow rate, we can estimate the other shear rate profiles for different flow rates using this ratio.

Effect of various values of the n-index

Figure 8 shows that the shear rates at the inner and outer walls decrease as the value of n-index increases. To maintain the same shear rate and elongation rate, the flow rate should also increase. According to the simulation results, the shear rate distribution is first concave and then convex for $n > 1$ but first convex and then concave for $n < 1$. The semianalytical results agree well with the CFD simulation results when the value of the n-index is between 0.703 and 1.423. Because the n-index of most polymer fluids lies within this range, the semianalytical solution derived in this study can be widely applied to most polymer fluids.

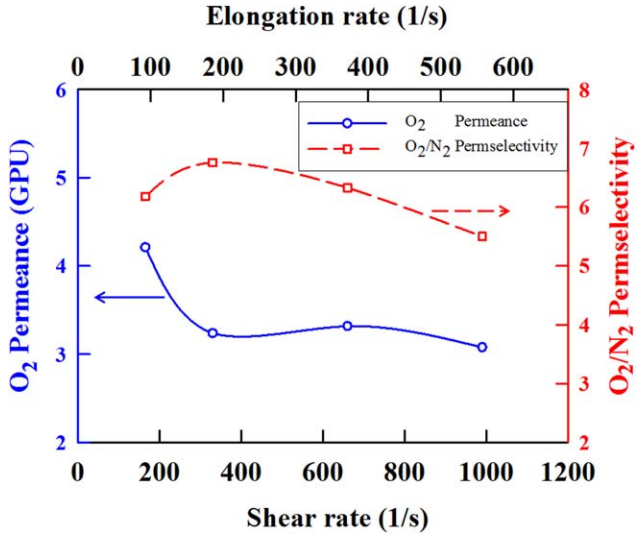

Figure 9. Relationships between gas separation performance and shear and elongation rates for hollow fiber membranes spun from a 60° spinneret (experimental data from Cao et al.[27]); permeance equals permeability divided by the thickness of the selective layer and is expressed in gas permeance units (GPU) with 1 GPU = 1 × 10^{-6} cm^3 (STP)/(cm^2-s-cmHg) = 3.3 × 10^{-1} mol/(m^2-s-Pa).

[Color figure can be viewed in the online issue, which is available at wileyonlinelibrary.com.]

Validation of the derived semianalytical solution

Since the separation performance of a hollow fiber is determined by the selective layer located at its outer wall, the elongation rate and shear rate at the outer wall of a spinneret outlet are important parameters directly influencing the selective layer. To validate the derived semianalytical solution, the separation performances of PES hollow fibers adopted from Cao et al.[27] were then plotted vs. the semianalytical shear rate and elongation rate as shown in Figure 9. According to the gas separation performances of PES hollow fibers wet-spun by a spinneret with a flow angle of 60°,[27] the shear rate and elongation rate are calculated through the semianalytical solution under each spinning condition. Under low dope flow rate, elongation

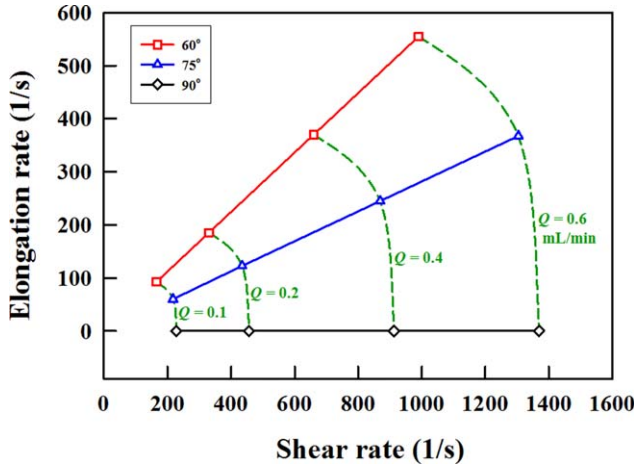

Figure 10. Elongation and shear rates at the outer wall of the outlet for various spinnerets and dope fluid flow rates.

[Color figure can be viewed in the online issue, which is available at wileyonlinelibrary.com.]

rate and shear rate enhanced monodispersity and the alignment of molecular chains, respectively, leading to a denser selective layer and a better permselectivity as shear rate and elongation rate increased. After the dope flow rate exceeds a critical point, the permselectivity decreases with shear rate and elongation rate otherwise. The decrease can be attributed to the significant decrease in viscosity of shear-thinning polymer doping at higher shear and elongation rates. Therefore, instead of time-consuming simulation, the effect of both shear and elongation rates on the gas separation performances can be quickly obtained with the aid of semianalytical solution derived in this study with specified experimental parameters.

Figure 10 generalizes the elongation and shear rates at the outer wall of the outlet for various spinnerets and dope fluid flow rates. Both shear and elongation rates are linearly proportional to the dope fluid flow rates for each spinneret. Before reaching the critical point, the permselectivity can be enhanced by increasing either shear rate or elongation rate of dope fluids as revealed in the literature.[27] However, there is a trade-off between shear rate and elongation rate. To spin a hollow fiber membrane with a desired separation performance, Figure 10 provides a reference for material engineers to choose a desirable spinneret.

Conclusions

By introducing an angle coefficient, a semianalytical solution was derived for a power-law fluid flowing through a conical annulus. Accounting for the effect of radial flow, the angle coefficient correctly modifies the governing equation for the power-law fluid flowing through the straight annulus. Given all six variables (Q, κ, ξ, ζ, ε and n) that determine a spinneret system, we can readily estimate the z-velocity profile, shear rate, and elongation rate within the spinneret from the semianalytical solution derived in this study. Furthermore, the results obtained from the semianalytical solution are in good agreement with those calculated by CFD simulations, validating our work. For a power-law fluid of $n = 1.423$ flowing through a 60° spinneret at a rate of 0.2 mL/min, the wall shear stresses derived in this study deviate from the CFD simulation results by approximately 10%. Using the semianalytical solution derived in this study, we can accurately estimate the shear rate and the elongation rate when designing a spinneret structure to spin a hollow fiber membrane with optimal separation performance.

Acknowledgments

The authors would like to thank the Ministry of Science and Technology (MOST), R.O.C. for their financial supports with project numbers 101-2815-C-033-008-E, 102-2221-E-002-033-MY3, and 103-2622-E-002-003-CC1.

Notations

A = parameter of the angle coefficient
B = parameter of the angle coefficient
m = power-law model consistency, Pa•s^n
n = power-law index, dimensionless
P = pressure, Pa
Q = flow rate of the dope fluid, m^3/s
Q_i = flow rate of the dope fluid for Section i, with $i \in$ (I, II), m^3/s
R = outer radius of the annulus of Section I in Figure 1, m
r = radial coordinate, m
s = power-law constant, dimensionless
T = temperature, K
t = time, s
V_i = velocity of fluid along the i-coordinate direction, with $i \in (r, z)$, m/s
v = velocity of fluid, m/s
z = axial coordinate, m

Greek letters

α = dimensionless radius for the outlet tube of Section II in Figure 1
β = dimensionless length for Section II in Figure 1
$\dot{\gamma}$ = shear rate, 1/s
δ = dimensionless radius for the outer converging tube of Section II in Figure 1
ε = slope of the converging section in a converging annulus
ζ = dimensionless variable for axial coordinate
η = dimensionless axial coordinate based on βR
θ = angular coordinate
κ = dimensionless radius for the inner tube of the spinneret in Figure 1
λ = dimensionless radial position at which the shear stress vanishes
μ = apparent viscosity of non-Newtonian-power-law fluid, Pa•s
ξ = dimensionless variable for r-coordinate based on R
ρ = density, kg/m^3
τ = shear stress, N/m^2
ϕ = angle coefficient, dimensionless
ψ = dimensionless radial coordinate excluding radial dimension of inner tube

Literature Cited

1. Wang P, Chung TS. Exploring the spinning and operations of multi-bore hollow fiber membranes for vacuum membrane distillation. *AIChE J*. 2014;60:1078–1090.
2. Ekiner OM, Vassilatos G. Polyaramide hollow fibers for H2/CH4 separation II. *spinning and properties*. *J Membr Sci*. 2001;186:71–84.
3. Miao XQ, Sourirajan S, Zhang H, Lau WWY. Production of polyethersulfone hollow fiber ultrafiltration membranes. Part I. Effects of water (internal coagulant) flow rate (WFR) and length of air gap (LAG). *Sep Sci Technol*. 1996;31:141–172.
4. Vanthof JA, Reuvers AJ, Boom RM, Rolevink HHM, Smolders CA. Preparation of asymmetric gas separation membranes with high selectivity by a dual-bath coagulation method. *J Membr Sci*. 1992; 70:17–30.
5. Chung TS, Teoh SK, Hu XD. Formation of ultrathin high-performance polyethersulfone hollow-fiber membranes. *J Membr Sci*. 1997;133:161–175.
6. Wang KY, Chung TS. Polybenzimidazole nanofiltration hollow fiber for cephalexin separation. *AIChE J*. 2006;52:1363–1377.
7. Bonyadi S, Chung TS, Rajagopalan R. A novel approach to fabricate macrovoid-free and highly permeable PVDF hollow fiber membranes for membrane distillation. *AIChE J*. 2009;55:828–833.
8. Ismail AF, Lau WJ. Theoretical studies on structural and electrical properties of PES/SPEEK blend nanofiltration membrane. *AIChE J*. 2009;55:2081–2093.
9. Xu ZL, Chung TS, Huang Y. Effect of polyvinylpyrrolidone molecular weights on morphology, oil/water separation, mechanical and thermal properties of polyetherimide/polyvinylpyrrolidone hollow fiber membranes. *J Appl Polym Sci*. 1999;74:2220–2233.
10. Chung TS, Kafchinski ER, Vora R. Development of a defect-free 6FDA-durene asymmetric hollow fiber and its composite hollow fibers. *J Membr Sci*. 1994;88:21–36.
11. Cabasso I, Klein E, Smith JK. Polysulfone hollow fiber. *II. Morphology*. *J Appl Polym Sci*. 1977;21:165–180.
12. Wang DL, Li K, Teo WK. Polyethersulfone hollow fiber gas separation membranes prepared from NMP/alcohol solvent systems. *J Membr Sci*. 1996;115:85–108.
13. Aptel P, Abidine N, Ivaldi F, Lafaille JP. Polysulfone hollow fibers-effect of spinning conditions on ultrafiltration properties. *J Membr Sci*. 1985;22:199–215.
14. Chung TS, Teoh SK, Lau WWY, Srinivasan MP. Effect of shear stress within the spinneret on hollow fiber membrane morphology and separation performance. *Ind Eng Chem Res*. 1998;37:3930–3938.
15. Chung TS, Teoh SK, Lau WWY, Srinivasan MP. Effect of shear stress within the spinneret on hollow fiber membrane morphology and separation performance. *Ind Eng Chem Res*. 1998;37:4903–4903.

16. Chung TS, Lin WH, Vora RH. The effect of shear rates on gas separation performance of 6FDA-durene polyimide hollow fibers. *J Membr Sci*. 2000;167: 55–66.
17. Qin JJ, Wang R, Chung TS. Investigation of shear stress effect within a spinneret on flux, separation and thermomechanical properties of hollow fiber ultrafiltration membranes. *J Membr Sci*. 2000; 175:197–213.
18. Qin JJ, Chung TS. Effect of dope flow rate on the morphology, separation performance, thermal and mechanical properties of ultrafiltration hollow fibre membranes. *J Membr Sci*. 1999;157:35–51.
19. Chung TS, Qin JJ, Gu J. Effect of shear rate within the spinneret on morphology, separation performance and mechanical properties of ultrafiltration polyethersulfone hollow fiber membranes. *Chem Eng Sci*. 2000;55:1077–1091.
20. Xue G, Jiang SG, Dai CP, Zhu W, Seng RP. Characterization of orientation at polyester fiber surface by modified infrared reflection technique. *Polym Bull*. 1986;15:363–368.
21. Ismail AF, Shilton SJ, Dunkin IR, Gallivan SL. Direct measurement of rheologically induced molecular orientation in gas separation hollow fibre membranes and effects on selectivity. *J Membr Sci*. 1997; 126:133–137.
22. Idris A, Ismail AF, Noorhayati M, Shilton SJ. Measurement of rheologically induced molecular orientation using attenuated total reflection infrared dichroism in reverse osmosis hollow fiber cellulose acetate membranes and influence on separation performance. *J Membr Sci*. 2003;213:45–54.
23. Fredrickson AG, Bird RB. Non-Newtonian flow in annuli. *Ind Eng Chem*. 1958;50:347–352.
24. Shilton SJ. Flow profile induced in spinneret during hollow fiber membrane spinning. *J Appl Polym Sci*. 1997;65:1359–1362.
25. Wang KY, Matsuura T, Chung TS, Guo WF. The effects of flow angle and shear rate within the spinneret on the separation performance of poly (ethersulfone) (PES) ultrafiltration hollow fiber membranes. *J Membr Sci*. 2004;240:67–79.
26. Widjojo N, Chung T-S, Arifin DY, Weber M, Warzelhan V. Elimination of die swell and instability in hollow fiber spinning process of hyperbranched polyethersulfone (HPES) via novel spinneret designs and precise spinning conditions. *Chem Eng J*. 2010;163(1–2):143–153.
27. Cao C, Chung TS, Chen SB, Dong ZJ. The study of elongation and shear rates in spinning process and its effect on gas separation performance of Poly(ether sulfone) (PES) hollow fiber membranes. *Chem Eng Sci*. 2004;59:1053–1062.
28. Li YL, Tung KL. CFD simulation of fluid. flow through spacer-filled membrane module: selecting suitable cell types for periodic boundary conditions. *Desalination*. 2008;233:351–358.
29. Li Y-L, Tung KL. The effect of curvature of a spacer-filled channel on fluid flow in spiral-wound membrane modules. *J Membr Sci*. 2008;319:286–297.
30. Li Y-L, Tung KL, Lu MY, Huang SH. Mitigating the curvature effect of the spacer-filled channel in a spiral-wound membrane module. *J Membr Sci*. 2009;329:106–118.
31. Duran JE, Mohseni M, Taghipour F. Computational fluid dynamics modeling of immobilized photocatalytic reactors for water treatment. *AIChE J*. 2011;57:1860–1872.
32. Kim AS, Lee YT. Laminar flow with injection through a long dead-end cylindrical porous tube: application to a hollow fiber membrane. *AIChE J*. 2011;57:1997–2006.
33. Tung KL, Li YL, Hu CC, Chen YS. Power-Law polymer solution flow in a converging annular spinneret: analytical approximation and numerical computation. *AIChE J*. 2012;58:122–131.
34. Li YL, Tung KL, Chen YS, Hwang KJ. CFD analysis of the initial stages of particle deposition in spiral-wound membrane modules. *Desalination*. 2012;287:200–208.
35. Li YL, Lin PJ, Tung KL. CFD analysis of fluid flow through a spacer-filled disk-type membrane module. *Desalination*. 2011;283: 140–147.

Manuscript received Feb. 19, 2015, and revision received Apr. 20, 2015.